JACS
JOURNAL OF THE AMERICAN CHEMICAL SOCIETY
pubs.acs.org/JACS
Article

Computational Discovery of Stable Metal−Organic Frameworks for Methane-to-Methanol Catalysis

Husain Adamji, Aditya Nandy, Ilia Kevlishvili, Yuriy Román-Leshkov, and Heather J. Kulik*

Cite This: https://doi.org/10.1021/jacs.3c03351
Read Online

ABSTRACT: The challenge of direct partial oxidation of methane to methanol has motivated the targeted search of metal−organic frameworks (MOFs) as a promising class of materials for this transformation because of their site-isolated metals with tunable ligand environments. Thousands of MOFs have been synthesized, yet relatively few have been screened for their promise in methane conversion. We developed a high-throughput virtual screening workflow that identifies MOFs from a diverse space of experimental MOFs that have not been studied for catalysis, yet are thermally stable, synthesizable, and have promising unsaturated metal sites for C−H activation via a terminal metal-oxo species. We carried out density functional theory calculations of the radical rebound mechanism for methane-to-methanol conversion on models of the secondary building units (SBUs) from 87 selected MOFs. While we showed that oxo formation favorability decreases with increasing 3d filling, consistent with prior work, previously observed scaling relations between oxo formation and hydrogen atom transfer (HAT) are disrupted by the greater diversity in our MOF set. Accordingly, we focused on Mn MOFs, which favor oxo intermediates without disfavoring HAT or leading to high methanol release energies—a key feature for methane hydroxylation activity. We identified three Mn MOFs comprising unsaturated Mn centers bound to weak-field carboxylate ligands in planar or bent geometries with promising methane-to-methanol kinetics and thermodynamics. The energetic spans of these MOFs are indicative of promising turnover frequencies for methane to methanol that warrant further experimental catalytic studies.

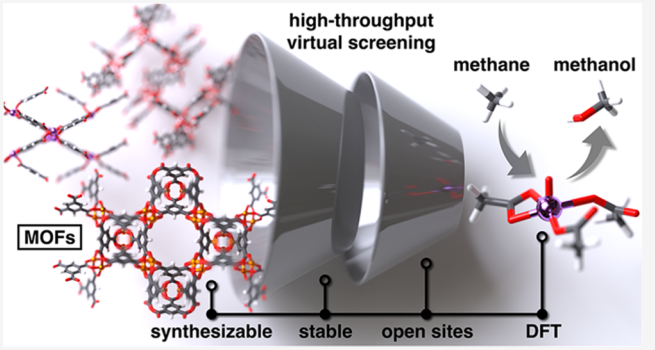

1. INTRODUCTION

While the abundance of natural gas has motivated the valorization of methane as an energy feedstock,[1] direct use of methane for the production of higher-value chemicals like methanol is limited by the lack of successful strategies for selective partial methane oxidation.[1,2] A limiting factor is the high C−H bond dissociation energy in methane compared to the partially oxidized products, which leads to overoxidation.[3−6] Instead, energy-intensive routes that first produce syngas from methane at very high operating temperatures and pressures are customarily used in industry.[7−10] Living systems leverage metalloenzymes such as soluble methane monooxygenase (sMMO) to convert methane selectively into methanol under ambient conditions using molecular oxygen as the oxidant[11−13] by forming, for example, a mononuclear Fe(IV)=O species that activates methane.[14−16] These metalloenzymes have inspired the design of synthetic homogeneous and heterogeneous catalysts for the direct conversion of methane to methanol via more energy-efficient methods.[17−25] Nevertheless, no synthetic catalyst to date is capable of simultaneously achieving high conversions and selectivities as enzymes have, motivating a wider search of candidate catalysts.

Porous materials, such as metal−organic frameworks (MOFs), are an attractive target for bioinspired heterogeneous catalyst design.[26−29] The well-defined metal sites contained in the secondary building unit (SBU) of the reticular MOF structure[30,31] have structural and electronic features that are analogous to the metal cofactors in metalloenzymes,[32] including weaker-field ligands that favor high-spin electron configurations that are needed for redox-mediated reactions,[32,33] as well as pore architectures that resemble an enzyme's binding pocket.[21,34] Inspired by sMMO, zeolites containing open Fe sites in the square planar geometry[35−37] and subsequently, MOFs with SBUs containing open Fe sites in the square pyramidal geometry[38−40] have demonstrated C−H activation activity in light alkanes (i.e., ethane and propane). Additionally, MOFs have been used as scaffolds with metal active sites that are active for alkane hydroxylation incorporated in the pore via postsynthetic functionalization methods.[41−43] The enhancement of methanol selectivity in

Received: March 31, 2023

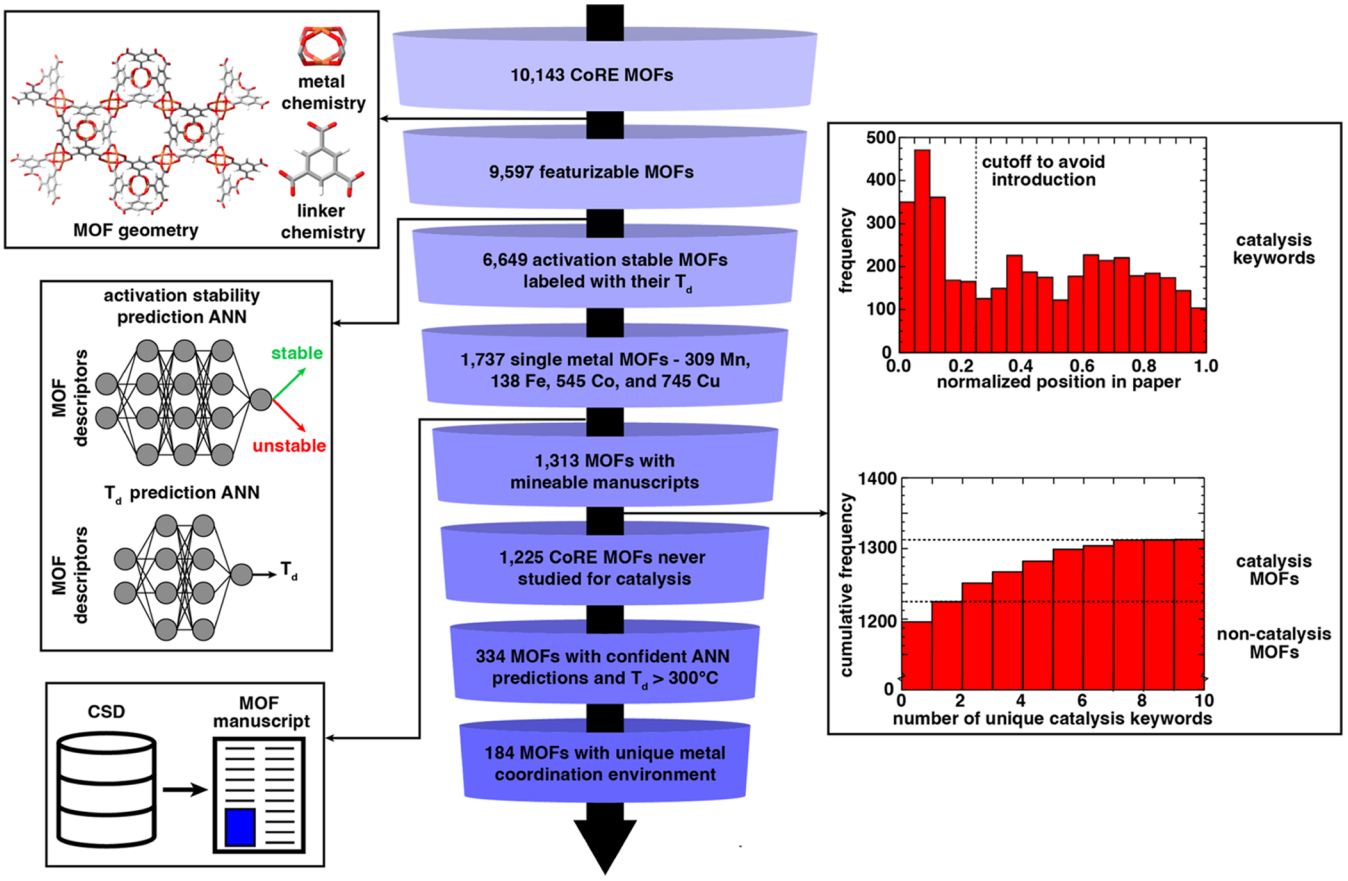

Figure 1. Workflow to repurpose synthesized MOFs for catalytic applications. Starting with the sanitized MOF structures contained in the CoRE MOF database, we eliminate MOFs that cannot be featurized. We then apply ANN-based activation and thermal stability prediction models to determine activation-stable MOFs and their corresponding decomposition temperatures and narrow our space down to MOFs containing a single transition-metal element corresponding to Mn, Fe, Co, or Cu. This is followed by text mining of the MOF manuscripts to identify CoRE MOFs not previously studied for catalysis. Next, we only retain MOFs with confident activation stability and decomposition temperature predictions based on uncertainty quantification metrics that have decomposition temperatures greater than 300 °C. Finally, we eliminate MOFs with identical metal-centered features.

such systems is typically achieved by solvent-aided methanol desorption (e.g., using H_2O) from the active metal site to prevent its overoxidation.[24,25,39,41,44] Nevertheless, the discovery of new MOFs capable of selective C−H activation requires tedious iterative trial and error workflows. There are thousands of candidate MOFs that could be experimentally synthesized and tested for catalytic activity, which can be extremely time-consuming. Furthermore, evidence of catalytic activity on candidate MOFs must be accompanied by detailed mechanistic studies that capture fleeting intermediates in the catalytic cycle with *in situ* spectroscopy, which can prove challenging for MOFs.[45−47]

First-principles calculations have thus played a vital role in understanding MOF catalysis,[28,48] especially in deciphering reaction mechanisms,[49] active site structures,[25,42] and the roles of the chemical environment[50] in C−H activation by MOFs. While computation has been valuable in rationalizing the activity of MOFs known to be capable of selective C−H activation, computation can play a leading role by enabling high-throughput virtual screening (HTVS) on the large chemical space of synthesized MOFs.[51,52] Such HTVS campaigns have been carried out[53−55] but have typically targeted specific metal coordination geometries in the MOF SBUs.[55−57] Notably, most screening efforts overlook MOF stability as a design criterion, which is critical for thermal catalysis.[58] Linear free energy relationships (LFERs)[59−61] are often exploited to accelerate catalyst HTVS[62−64] by drawing correlations between readily computed descriptors and the energetics of individual intermediates or reaction steps.[55−57,65−69] LFERs, however, have been shown to be disrupted by changes to the catalyst structure,[70−72] non-covalent interactions that selectively stabilize specific reaction intermediates,[50,72,73] or when probing chemical spaces with greater diversity in metal identity, oxidation, and spin states.[74,75] Thus, it is necessary both to expand the search for MOFs beyond those that have been previously studied computationally or experimentally and to identify MOFs that may have been overlooked because of assumed LFERs that may not hold.

In this work, we developed an HTVS workflow that combines previously developed machine learning[58,76] models with DFT to repurpose synthesized MOFs with moderate thermal stability that have not yet been studied experimentally for direct methane-to-methanol catalysis. We used DFT to compute reaction energetics for the complete methane-to-methanol catalytic cycle and show that LFERs fail to generalize across diverse chemical spaces of MOFs. We identified promising MOFs for future experimental studies by using this workflow to first select MOF candidates with good reaction energetics across the catalytic cycle and then compute

https://doi.org/10.1021/jacs.3c03351
J. Am. Chem. Soc. XXXX, XXX, XXX−XXX

their full energy landscapes to confirm both their thermodynamic and kinetic feasibility for methane-to-methanol catalysis.

2. RESULTS AND DISCUSSION

2.1. Repurposing Synthesized MOFs for Methane-to-Methanol Catalysis. The primary factor limiting the application of MOFs in catalysis is their poor stability. Here, we considered a MOF stable and suitable for catalysis if it is activation stable, i.e., maintains its structural integrity following solvent removal from its pores during activation, and is thermally stable, i.e., shows resilience under elevated temperatures typical in thermal catalysis (e.g., above 200 °C).[77,78] We apply two different artificial neural network (ANN) models developed in prior work[58] that were trained on extant MOF experimental literature and rely on connectivity-based revised autocorrelations (RACs) and geometric descriptors computed on the unoptimized MOF periodic structure as input. The first model is a binary classifier that predicts whether a MOF is stable after removal of solvent from its pores during the activation process (activation stability ANN) and the second model is a regressor that predicts the thermogravimetric analysis (TGA) decomposition temperature of a MOF (thermal stability ANN). We start with the 10,143 non-disordered MOF structures in the 2019 Computation-Ready, Experimental All Solvent Removed (CoRE ASR) MOF database v.1.1.2[79] and retain 9,597 MOFs that are compatible with our featurization as discussed in prior work.[58,76] The activation stability ANN is first applied to the set of featurizable MOFs, and predicts that 69.3% (6,649 MOFs) are stable upon activation (Figure 1). For all activation-stable MOFs, we subsequently predict their corresponding thermal decomposition temperatures using the thermal stability ANN and limit our analysis to MOFs containing a single transition-metal element corresponding to Mn, Fe, Co, or Cu, reducing our set to 1,737 MOFs (Figure 1). We focus on these transition metals because they have been used for methane-to-methanol catalysis in biological, homogeneous, and heterogeneous systems.[23,24,75,80] We limited our study to MOFs containing a single transition-metal element to avoid studying systems with potential bifunctional catalytic sites that would be ambiguous to model (see Sections 2.2 and 4) or for which it would be difficult to predict which transition-metal center is the catalytically active species.

Next, we employed text mining methods[58,76,81,82] to further screen our CoRE MOF dataset for candidates that have not been studied for catalysis but are activation-stable. Of the 1,737 single-metal activation-stable MOFs, 1,313 MOFs have downloadable manuscripts in our corpus curated from the CSD in prior work (Figure 1).[58,76] We built a list of catalysis-specific keywords and used keyword matching with the corresponding manuscripts to identify whether a MOF has been studied for catalysis (Supporting Information Table S1). We ignored keyword matches that appear in the Introduction section because authors typically highlight catalysis as a practical application for MOFs without studying the MOFs of interest for catalysis. For the introduction, we selected a cutoff of the first 25% of the manuscript, a heuristic chosen by trial and error (Figure 1). We label a CoRE MOF as not used for catalysis if its manuscript has fewer than 3 keyword matches after the introduction (Figure 1 and Supporting Information Table S2). We identify 1,225 single-metal CoRE MOFs that have not been tested experimentally for catalysis despite being predicted or reported to have activation stability.

For suitability in thermal catalysis, a MOF must be stable at high temperatures. The average thermal decomposition temperature from the experimental TGA dataset used to train the thermal stability ANN was 359 °C, which corresponds to the lower limit of decomposition temperatures for stable MOFs.[58] We sought MOFs that contain first-row transition metals with moderate thermal stability for catalytic applications and used a thermal decomposition temperature cutoff of 300 °C on our predicted decomposition temperatures from the thermal stability ANN, which narrowed our dataset to 733 MOFs that are both stable upon activation and have thermal stability but have not been studied experimentally for catalysis. Although the decomposition temperature from a TGA measurement may be expected to be an overestimate of the temperature at which the material may break down during catalytic conditions, our use of a relatively high cutoff for thermal stability should still yield MOFs with stabilities suitable for catalysis at elevated (e.g., 200 °C) temperatures. Retaining only MOFs with confidently predicted activation and thermal stabilities by applying uncertainty quantification metrics to predictions from both our ANN models,[58] our dataset was reduced to 334 MOFs (Supporting Information). Of this set, 58% had an experimental ground truth from the TGA dataset and 54% were unseen by the thermal stability ANN training data (i.e., because they were unavailable or were in the test partition, Supporting Information Table S3). Next, we identified MOFs with identical metal-centered RACs as these would have equivalent metal coordination environments (Figure 1). We retained only the MOF with the highest decomposition temperature prediction for MOFs with identical metal coordination environments to avoid redundant calculations on MOF SBU cluster models, reducing our dataset to 184 MOFs (Figure 1).

Next, we used MOFSimplify[76] to extract the SBUs from their periodic structures and computed atomic-weighted molecular graph determinants[83] of each extracted SBU to retain a single copy of each unique SBU for each MOF (i.e., as judged by connectivity), with the 184 MOFs yielding 242 unique SBUs (Figure 2). We expect that a metal site in an SBU can only be catalytically active for methane-to-methanol catalysis if it is an open metal site (i.e., for a 3d transition metal, the coordination number cannot exceed five). We computed the coordination number of each metal site across all 242 SBUs, automatically categorizing metal sites with coordination numbers 2 and 3 as being open sites. Because metal sites with coordination numbers 4 or 5 are ″open″ only for certain geometries, we performed a geometry index analysis[84,85] and used heuristic cutoffs to identify open sites (Supporting Information Figure S1). Our workflow retained SBUs with at least one open metal site available for reactivity (Figure 2).

We studied the formation of a terminal metal-oxo species at the open metal site because these have been found to be capable of C−H activation,[36,38,39,75] but SBUs with multiple metal centers that have strong metal−metal interactions could favor the formation of other metal-oxygen species (e.g., bridged μ-metal-oxo). To reduce the likelihood of identifying SBUs with these preferred intermediates, we computed formal shortness ratios (FSR)[86] for all possible pairs of metals in each SBU with more than one metal site (Supporting Information Figure S2). We eliminated SBUs with an FSR of <1.1, which is a conservative threshold for identifying SBUs with strong metal−metal interactions.[87] This resulted in 144 SBUs

https://doi.org/10.1021/jacs.3c03351
J. Am. Chem. Soc. XXXX, XXX, XXX−XXX

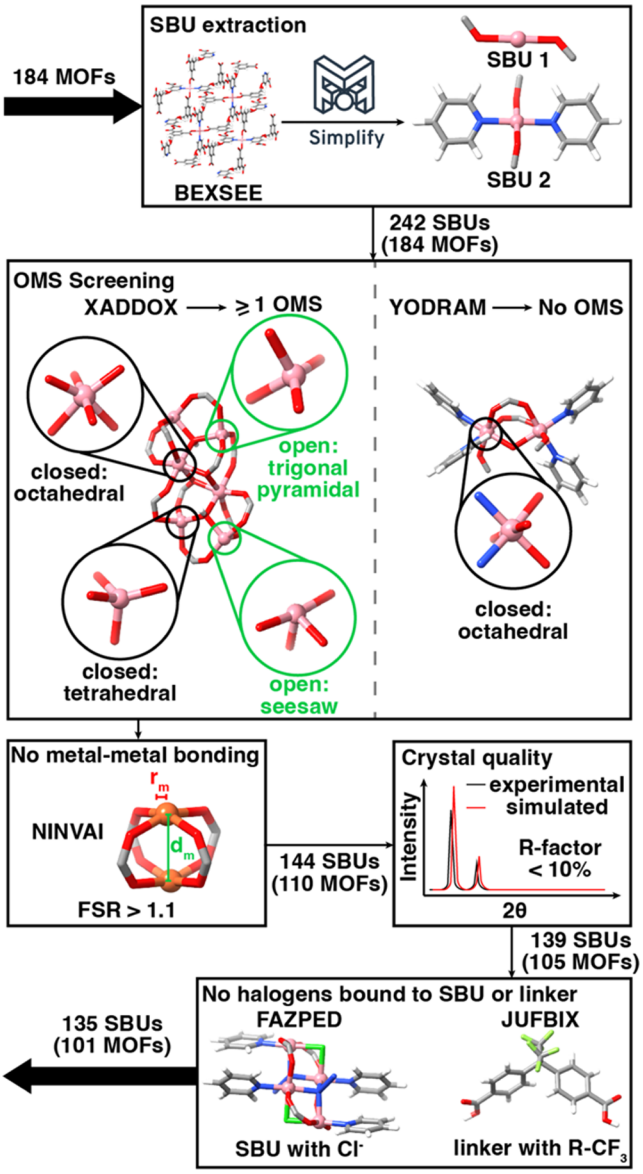

Figure 2. Screening for open metal sites (OMSs) capable of terminal metal-oxo formation for methane-to-methanol catalysis. MOFSimplify is used to extract unique SBUs from the single-metal MOFs identified as stable for catalytic applications. Only SBUs with at least one open metal site are retained. For SBUs containing the same element in multiple metal sites in a configuration in which at least one corresponds to an open metal site, we only retain those with FSR values between all possible metal pairs exceeding 1.1. Next, we filter for good crystal quality, keeping the SBUs of MOFs with *R*-factors less than 10%. Lastly, we eliminate any MOFs and their corresponding SBUs that have halogens bound to the SBU or linker. Atoms are colored as follows: Co in pink, Fe in orange, O in red, N in blue, C in gray, H in white, Cl in light green, F in yellow-green.

corresponding to 110 MOFs with open metal sites capable of terminal metal-oxo formation (Figure 2). Lastly, we applied two additional filters in our MOF screening workflows based on practical considerations. We eliminated MOFs that have poor crystal quality based on their *R*-factors, which is a measure of agreement between the crystallographic model of a MOF and its experimental X-ray diffraction data,[88] as well as MOFs containing halogens bound to the linker or SBU (Figure 2 and Supporting Information Text S1).[50] Therefore, our final dataset comprised 101 CoRE MOFs (135 SBUs) that are stable and have the potential to be repurposed for methane-to-methanol catalysis.

2.2. Reaction Mechanism and Modeling Approach. We first study the thermodynamics for the radical rebound mechanism[89] of methane-to-methanol catalysis occurring on cluster models of the SBUs whose metal centers serve as the active sites within the identified MOFs. To avoid magnetic coupling between adjacent transition-metal centers, models of the SBUs with multiple transition-metal centers were modified by replacing all but one transition-metal center with closed-shell Mg(II) ions (Supporting Information Tables S4–S6 and Figure S3). DFT calculations performed on representative Mn- and Fe-based MOF SBUs with multiple transition-metal centers where only one metal center served as the active site showed that trends in relative energetics were qualitatively unchanged in comparison to the same SBUs with Mg substitution (Supporting Information Table S5). Mg-substituted SBU models with equivalent connectivity are removed. Such an approach has been previously validated for MOFs with weak to moderate coupling between metal centers (e.g., Fe-MOF-74),[49] and we expect our MOFs to be predominantly in this coupling limit due to our criteria for only including MOFs with relatively high metal–metal separation (i.e., high FSR, see Sections 2.1 and 4). Using these MOF models, we first characterize reactive intermediates to estimate reaction thermodynamics for methane-to-methanol conversion. In this catalytic cycle, the coordinatively unsaturated transition-metal center in the resting state structure (**1**) of the MOF SBU undergoes two-electron oxidation to form a high-valent terminal metal-oxo species (**2**) using triplet molecular oxygen

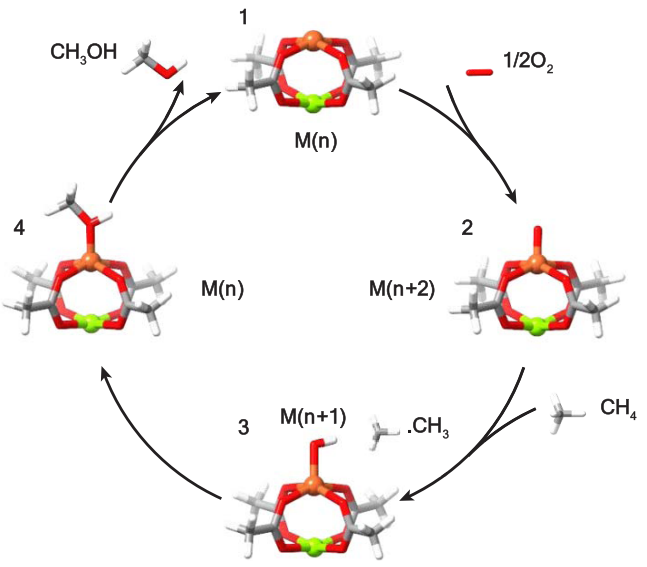

Figure 3. Radical rebound catalytic cycle for methane to methanol at the Fe active site of a representative MOF SBU (CSD refcode: NINVAI). Starting with the resting state (**1**) with the active metal at an oxidation state of *n*, the cycle proceeds in the clockwise direction to form the metal-oxo (**2**) species from triplet oxygen, the metal-hydroxo species (**3**) via HAT from methane, and the methanol-bound (**4**) species through methyl radical rebound. The nonreacting Fe atom has been replaced with Mg for the purpose of computational modeling. Color codes: orange—Fe, green—Mg, gray—C, red—O, white—H.

https://doi.org/10.1021/jacs.3c03351
J. Am. Chem. Soc. XXXX, XXX, XXX−XXX

as the source of the oxygen atom (Figure 3). The metal-oxo formation energy, $\Delta E(\text{oxo})$, is computed as

$$\Delta E(\text{oxo}) = E(\mathbf{2}) - E(\mathbf{1}) - \frac{1}{2}E(O_2)$$

Alternative oxidants (e.g., N_2O or H_2O_2) would rigidly shift reaction energies without affecting relative energetics (Supporting Information Table S7). The highly active terminal metal-oxo intermediate catalyzes a hydrogen atom transfer (HAT) step wherein a hydrogen atom is abstracted from methane to form a metal-hydroxo species (**3**) and a methyl radical (Figure 3). The associated reaction energy, $\Delta E(\text{HAT})$ is

$$\Delta E(\text{HAT}) = E(\mathbf{3}) + E(CH_3\bullet) - E(\mathbf{2}) - E(CH_4)$$

The methyl radical then rebounds onto the metal-hydroxo species (**3**) to form a methanol-bound intermediate (**4**) which is followed by the release of methanol to regenerate the resting state structure (**1**) (Figure 3). The reaction energy $\Delta E(\text{release})$ is given by

$$\Delta E(\text{release}) = E(\mathbf{1}) + E(CH_3OH) - E(\mathbf{4})$$

The resting oxidation states of the metals in the MOF SBUs were based on those reported in the manuscript associated with the Cambridge Structural Database (CSD) entry, except for Cu. In the case of Cu, we instead assigned a resting oxidation state of +2 even in cases of user-reported oxidation states of +1 due to the unreactive nature of the Cu(I) d^{10} ground state (Supporting Information Table S8). The combined metal oxidation state and charge on the ligands or linkers in the MOF SBUs (see Section 4) are used to assign the total charge of each SBU. For each metal, we selected the highest possible spin state that is accessible across all intermediates in the radical rebound cycle while ensuring that the spin state is conserved throughout the cycle (Supporting Information Table S9).[75] An α-radical transfer was selected for HAT in the generation of the metal-hydroxo species from the metal-oxo species.[75]

2.3. Global Trends in Methane-to-Methanol Reaction Energies. Given the widespread use of reaction-specific LFERs in catalysis,[3,55,65] we investigate whether a diverse design space of MOF SBUs follows energetic trends expected from established LFERs for the radical rebound mechanism of methane-to-methanol catalysis. First, we examine the overall and metal-specific trends in $\Delta E(\text{oxo})$ reaction energies across all SBUs of the selected CoRE MOFs. The $\Delta E(\text{oxo})$ values span a very wide range (ca. 190 kcal/mol) that are distributed by metal (Figure 4). We find that $\Delta E(\text{oxo})$ favorability is ordered by d-filling, with Mn MOFs forming the most stable metal-oxo intermediates (ca. −71 to 15 kcal/mol) followed by Fe MOFs (ca. 5−20 kcal/mol), Co MOFs (ca. −97 to 93 kcal/mol), and Cu MOFs (ca. 11−69 kcal/mol), respectively (Figure 4). The range of $\Delta E(\text{oxo})$ for Co SBUs is very wide compared to the other metals primarily due to two outliers at each extremum (Figure 4). Omitting the Co SBU outliers, the ordering of $\Delta E(\text{oxo})$ energies aligns with the oxo-wall theory that is applicable to tetragonal transition metal-oxo complexes,[90] although our MOF SBUs have a greater variation in coordination geometries than those that were used to propose the oxo-wall theory, which also allows for the possibility of terminal metal-oxo formation on 3d metals beyond the oxo-wall (Supporting Information Figure S4). Consistent with this theory, late transition metal-oxo complexes formed on MOF SBUs are thermodynamically unstable because they have lower formal metal-oxo bond orders (Supporting Information Figure S5). Thus, within our curated dataset, we identify previously overlooked Mn MOFs that form more stable metal-oxo intermediates than those formed by Fe MOFs.

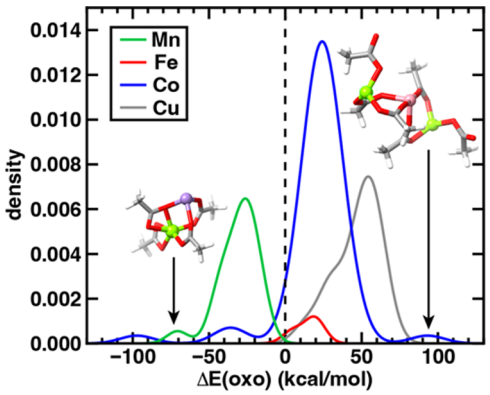

Figure 4. 1D Kernel density estimation (KDE) plot of the distributions of $\Delta E(\text{oxo})$ reaction energies in kcal/mol colored by metal: Mn in green, Fe in red, Co in blue, and Cu in gray. The dashed black vertical line corresponds to a zero value for $\Delta E(\text{oxo})$. The Mn SBU with the most favorable metal-oxo formation energy (CSD refcode: KUFVAK, $\Delta E(\text{oxo})$ = −70.7 kcal/mol) and the Co SBU with the least favorable metal-oxo formation energy (CSD refcode: TEDXOR, $\Delta E(\text{oxo})$ = 93.2 kcal/mol) are shown as insets. Only one catalytically active metal is studied in each of these SBUs, and the remaining metal sites are replaced with Mg for the purpose of computational modeling. Color codes: purple—Mn, pink Co, green—Mg, gray—C, red—O, white—H.

Prior work[55,57] on methane-to-methanol catalysis, which focused on MOF families with experimentally demonstrated O_2 chemisorption, showed that Fe MOFs exhibit the most favorable oxo formation. In this case, the studied MOFs usually shared a common structure, whereas our dataset includes more diverse coordination environments around the metal centers, leading to prediction of favorable oxo formation by the presently studied Mn MOFs. Our results also align with trends observed in transition-metal complexes where homogeneous Mn catalysts also form the metal-oxo species more favorably than Fe catalysts.[75]

We find that $\Delta E(\text{HAT})$ values span a narrower range compared to the $\Delta E(\text{oxo})$ values, with most SBUs having $\Delta E(\text{HAT})$ within a range of 0 ± 20 kcal/mol (Figure 5). Due to the existence of a universal nearly 1:1 Bronsted−Evans−Polanyi (BEP) relation between the HAT kinetic barrier height and $\Delta E(\text{HAT})$,[62,72,91,92] this also suggests that HAT from methane is relatively facile. However, we observe a very weak overall global correlation between $\Delta E(\text{oxo})$ and $\Delta E(\text{HAT})$ reaction energies (Pearson's r = −0.28, Figure 5). This lack of correlation has also been observed in transition-metal complexes, and has been attributed to variations caused by changing metal oxidation and spin states[75] or geometric distortions of the metal with respect to the ligands.[72] For MOFs typically studied in a single spin state, LFERs have been suggested for $\Delta E(\text{oxo})$ vs $\Delta E(\text{HAT})$ in direct methane-to-methanol conversion,[55] but our results show that they do not hold across all metals in our dataset.

The degree of correlation between the $\Delta E(\text{oxo})$ and $\Delta E(\text{HAT})$ reaction energies varies by metal. Notably, Cu SBUs show the strongest correlation (Pearson's r = −0.94) between the two reaction energies with a steep slope of −0.95

https://doi.org/10.1021/jacs.3c03351
J. Am. Chem. Soc. XXXX, XXX, XXX−XXX

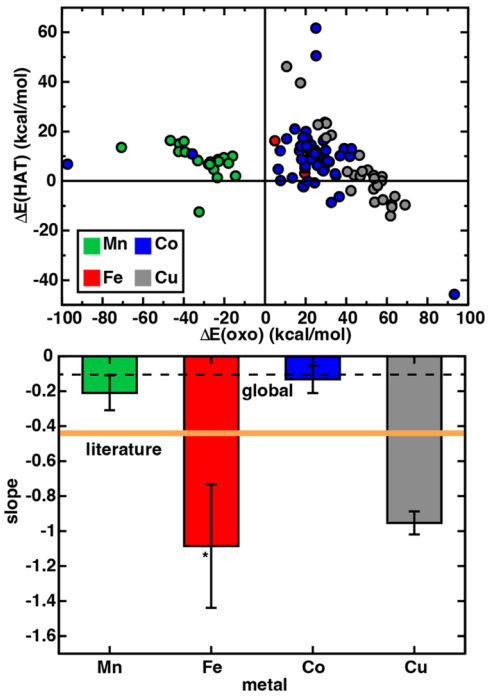

Figure 5. (Top) ΔE(HAT) as a function of ΔE(oxo) in kcal/mol for the SBUs in our set of activation and thermally stable MOFs for methane-to-methanol catalysis. The data points are colored by metal: Mn in green, Fe in red, Co in blue, and Cu in gray. (bottom) ΔE(oxo) vs ΔE(HAT) LFER slopes and standard errors per metal. The range of literature slopes is indicated by the shaded orange area, while the dashed black line corresponds to the slope of the global ΔE(oxo) vs ΔE(HAT) dataset over all MOFs. The asterisk for the Fe bar indicates that the slope was calculated from a small Fe dataset of size n = 3.

(Figure 5). We attribute this strong linear behavior to the formation of a terminal Cu-oxyl species on Cu SBUs instead of Cu-oxo intermediates, as observed from the relatively low Mayer bond valences[93] of the oxygen atom in their oxo intermediates (Supporting Information Figure S6). In contrast, the Mn SBUs show a weak correlation between ΔE(oxo) and ΔE(HAT) reaction energies (Pearson's r = −0.44) with a shallow slope of −0.21 (Figure 5). This suggests that the formation of a stable Mn-oxo species does not come at the cost of decreased HAT reactivity. We also observe limited overall and metal-specific correlation between the reaction energetics and quantum mechanical descriptors (e.g., frontier orbital energetics, spin density, and Mayer bond valence of the metal-oxo) commonly thought to predict C−H activation reactivity (Supporting Information Figures S7 and S8).[55,65] The lack of correlation of reaction energetics with underlying electronic descriptors provides further evidence for LFER disruption. Therefore, Mn MOFs appear to be highly promising for methane-to-methanol catalysis (Figure 5).

2.4. Proposing New Mn MOFs for Methane-to-Methanol Catalysis. The energy of methanol release, ΔE(release), is an important quantity in methane-to-methanol catalysis because it can become rate-limiting and is also indicative of methanol overoxidation in the presence of oxidant at the active site.[6,63,92] As discussed earlier, methanol release is commonly aided by a protonated solvent. However, in our release energy calculation, we do not incorporate solvent-facilitated desorption, meaning that the release energetics reported here are an upper bound and likely underestimate the catalyst performance. Nevertheless, we expect that relative catalyst performance within our set of studied MOFs is likely unchanged by this approximation. There is limited overall or metal-specific correlation between ΔE(release) and ΔE(oxo) or ΔE(HAT) (Figure 6). The methanol release energies are generally high across all SBUs regardless of metal (Figure 6). This could be due to the strong electrostatic attraction between the metal center and the bound methanol that is influenced by the overall positive charge on the SBU cluster

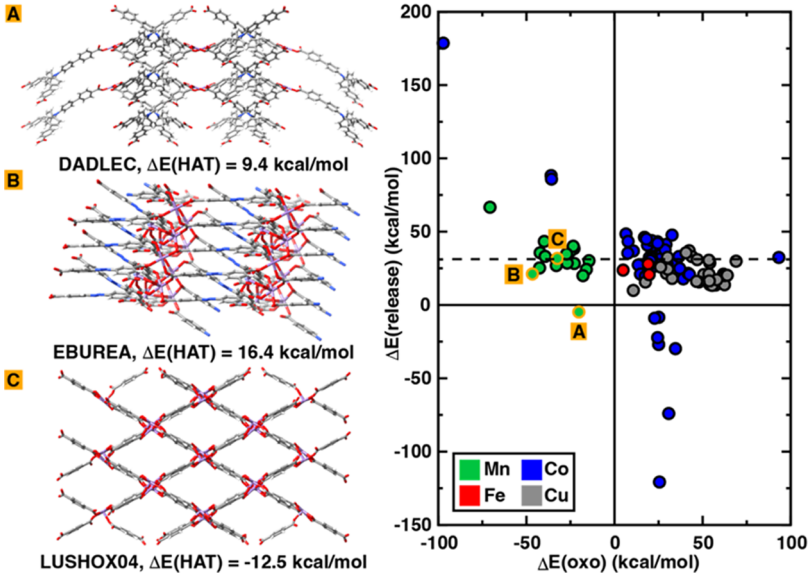

Figure 6. ΔE(release) as a function of ΔE(oxo) in kcal/mol for the SBUs in the set of 67 MOFs for which valid computational results were obtained. The data points are colored by metal: Mn in green, Fe in red, Co in blue, and Cu in gray. The black dashed line corresponds to ΔE(release) = 30 kcal/mol. Data points corresponding to the three Mn MOFs identified as most promising for methane-to-methanol catalysis are outlined in orange, and their associated periodic MOF structures are shown as insets with ΔE(HAT) values annotated. Color codes: purple—Mn, gray—C, red—O, white—H, blue—N.

https://doi.org/10.1021/jacs.3c03351
J. Am. Chem. Soc. XXXX, XXX, XXX−XXX

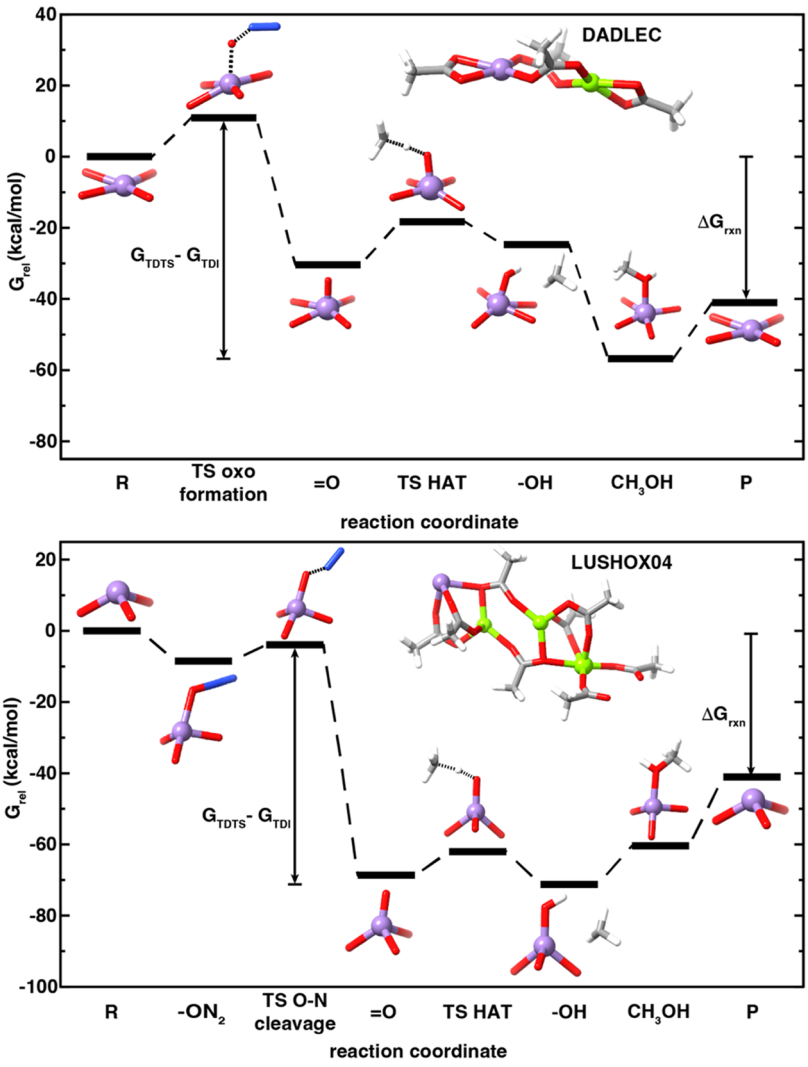

Figure 7. Gibbs free energy landscapes of (top) $Mn(HTPA)(DMF)_{2n}{\cdot}H_2O$ (CSD refcode DADLEC) and (bottom) $[Mn_2(BDC)_2(DMF)_2]_n$ (CSD refcode LUSHOX04) with SBU and active site structures shown as insets. We draw the reaction coordinate from the reactants (R) plus CH_4, and N_2O. DADLEC proceeds directly through an oxo formation TS (TS oxo formation) to form the metal-oxo intermediate (=O) while LUSHOX04 first forms a complex with N_2O ($-ON_2$), followed by an O−N bond cleavage TS (TS O−N cleavage) to form the metal-oxo intermediate (=O). The reaction coordinates then proceed through the HAT TS (TS HAT), the metal-hydroxo intermediate (−OH), the methanol-bound intermediate (CH_3OH), and products (P) comprising the SBU, CH_3OH, and N_2. The Gibbs free energy of reaction, ΔG_{rxn}, and the free energy differences between the TDTS and TDI are also shown. Only one catalytically active metal is studied in each of these SBUs, and the remaining metal sites are replaced with Mg for the purpose of computational modeling. Color codes: purple—Mn, green—Mg, gray—C, red—O, white—H, blue—N.

models.[92] The high methanol release energies are consistent with known challenges of methanol desorption from the active site.[75,94,95] We compare ΔE(oxo), ΔE(HAT), and ΔE(release) reaction energies in our dataset to those computed for Fe-MOF-74, which is known to catalyze ethane hydroxylation.[38,49] We find that Mn MOFs in our dataset form more stable metal-oxo intermediates than Fe-MOF-74 while having comparable HAT and methanol release energies (Supporting Information Figure S9 and Table S10). The substantial improvement in reaction energetics demonstrated by Mn MOFs, which exceeds the uncertainty associated with DFT, warrants experimental validation of their catalytic activity. Experimental testing would be feasible since these are all experimentally synthesized MOFs with well-documented synthesis procedures. Despite potential limitations in completing the catalytic cycle due to high methanol release energies, we identify three Mn MOFs with the most promising combination of ΔE(oxo), ΔE(HAT), and ΔE(release) for detailed characterization of the methane-to-methanol catalytic cycle. These three Mn MOFs are $[Mn(HTPA)(DMF)_2]_n{\cdot}H_2O$ (also referred to as FIR-34, CSD refcode DADLEC),[96] $[Mn_3(ABTC)_2(H_2O)_4{\cdot}9.5H_2O]_n$ (CSD refcode EBUREA),[97] and $[Mn_2(BDC)_2(DMF)_2]_n$ (CSD refcode LUSHOX04)[98] (Figure 6). These MOFs have been studied for their unique structural and magnetic properties but, to our knowledge, have yet to be tested for catalytic applications[96−98] or studied computationally. Additionally, these three MOFs exhibit both activation stability and high decomposition temperatures, as verified either from their corresponding manuscripts or according to our confident machine learning model predictions, while also having good mechanical stability based on their computed bulk elastic moduli[99] (Supporting Information Table S11).

For the three selected MOF SBUs, we characterize the full reaction coordinate (i.e., both transition states and reaction

https://doi.org/10.1021/jacs.3c03351
J. Am. Chem. Soc. XXXX, XXX, XXX−XXX

intermediates) with thermodynamic corrections for the radical rebound mechanism of methane-to-methanol catalysis using N_2O as an oxidant (Figure 7 and Supporting Information Texts S2 and S3 and Tables S12−S14). While we compute transition states for oxo formation and HAT, we model methanol release as an unassisted dissociation and so we neglect any kinetic barrier.[75,92,94] We also assume the rebound of the methyl radical following C−H activation to be barrierless[92] and omit explicit calculation of a barrier for this step.

The DADLEC MOF, which has a square planar geometry at the active Mn site, undergoes a concerted oxo formation step without the formation of a stable N_2O bound intermediate as confirmed by intrinsic reaction coordinate (IRC) calculations (Figure 7, Supporting Information Figure S10 and Text S2). The three-coordinate trigonal pyramidal Mn center in the SBU of LUSHOX04 instead exhibits stepwise oxo formation. Here, LUSHOX04 first forms a complex with N_2O, which is assumed to be barrierless since N_2O retains its linear geometry in this complex, followed by cleavage of the O−N bond to form the metal-oxo intermediate (Figure 7, Supporting Information Figure S11 and Text S2). The IRC calculations on EBUREA also suggest a stepwise oxo formation, but EBUREA forms a complex with N_2O in which N_2O assumes a bent geometry (Supporting Information Figures S12 and S13 and Text S2). Although we expect this complexation step to have a barrier due to the energetic cost of bending the N−N−O angle in N_2O,[100] we were unable to locate a transition state associated with complexation for EBUREA and thus do not consider this MOF further in our analysis.

We observe relatively low oxo formation barriers of 11 and 5 kcal/mol for DADLEC and LUSHOX04, respectively, indicating the facile formation of the active metal-oxo species for C−H activation of methane (Figure 7). We selected N_2O as the oxidant for calculating reaction coordinates due to difficulties mapping out a reaction coordinate in which molecular O_2 is split (i.e., with a co-reductant, as in enzyme catalysis,[12] or via multiple metal centers[80,101,102]). We nevertheless computed the energetics of O_2 chemisorption and found it to be favorable in these MOFs but at the cost of fairly high oxo formation barriers with O_2 when CO is used as a co-reductant (Supporting Information Text S2 and Figures S14−S17). This suggests the potential of the three identified Mn MOFs to use benign O_2 as the oxidant, perhaps in the presence of better co-reductants than CO. Both DADLEC and LUSHOX04 have C−H activation barriers of 12 kcal/mol and 7 kcal/mol, respectively, suggesting that the relatively easily formed metal-oxo species can also activate the strong C−H bonds in methane (Figure 7 and Supporting Information Figure S18). Thus, the computed free energy landscapes show that DADLEC and LUSHOX04 have both favorable kinetics and thermodynamics for methane-to-methanol catalysis.

We next applied the energetic span model to approximate catalytic turnover frequencies for DADLEC and LUSHOX04 in the presence of N_2O as the oxidant.[103] Both MOFs have the same turnover-determining transition state (TDTS) that is associated with the oxo formation step (Figure 7). The turnover-determining intermediate (TDI) for DADLEC is the expected methanol-bound intermediate (Figure 7). However, for LUSHOX04, the rebound step is slightly endergonic because the favorable enthalpy is outweighed by the loss of translational entropy. Thus, the TDI for LUSHOX04 is the hydroxo intermediate (Figure 7). The methanol release energy still defines one extremum of the energetic span for LUSHOX04, dictating the overall turnover frequency. The energetic span, ΔG for DADLEC and LUSHOX04 are 26.7 and 26.3 kcal/mol, respectively (Supporting Information Table S15). Despite the sensitivity of the quantitative free energy landscapes to the choice of functional, the energetic spans are qualitatively comparable to those on other MOF SBUs studied computationally for light alkane hydroxylation.[39,49,56,104] These promising computed turnover frequencies for methane-to-methanol catalysis merit further experimental validation through steady-state and transient kinetic studies.

3. CONCLUSIONS

We developed an HTVS workflow to guide the systematic discovery of MOF catalysts for the conversion of methane to methanol from a diverse space of materials. Unlike previous workflows, our approach mandated both MOF stability and synthesizability while identifying MOFs with promising unsaturated metal sites (i.e., Mn, Fe, Co, or Cu) amenable to forming a terminal metal-oxo for C−H activation. The components of our workflow designed to assess the satisfaction of these criteria can be readily adapted for HTVS of MOFs for other catalytic reactions since MOF stability, synthesizability, and availability of open metal sites are imperative to any catalytic process. To determine which of our materials were candidate catalysts specifically for methane hydroxylation, we carried out DFT calculations on 87 selected MOFs to determine methane-to-methanol reaction energetics following the radical rebound mechanism. In this work, we focus on metal-oxo formation energies, HAT energies, and methanol release energies, but our workflow can readily be expanded to construct off-cycle intermediates and probe energetics associated with other methane oxidation products which can provide insights on methanol selectivity. Despite significant metal-local structural diversity in our MOFs, the formation of oxo intermediates becomes less favorable with increasing 3d filling, as observed in octahedral metal complexes. At odds with prior work,[55,62] our diverse set indicates opportunities to disrupt scaling limitations between oxo formation and HAT. While metal-specific LFERs hold to varying degrees, Mn MOFs in particular have a weak ΔE(oxo) vs ΔE(HAT) correlation with a shallow slope. This suggests that favorable metal-oxo formation in Mn MOFs does not correlate to an energetic penalty for HAT, unlike in more commonly pursued Fe MOFs, indicating that Mn MOFs could be promising for methane-to-methanol conversion.

We showed that methanol release energetics are nearly completely uncorrelated to the other two steps, requiring its explicit consideration when selecting the best MOF candidates for catalysis. Taking release energetics into account, we identified three Mn MOFs with the most promising methane-to-methanol thermodynamics (CSD refcodes DADLEC, EBUREA, and LUSHOX04). We computed the full free energy landscapes of these MOFs using N_2O as the oxidant and observed relatively low oxo formation barriers and HAT barriers, suggesting good propensity for C−H activation. Furthermore, the computed energetic spans for these MOFs, which are related to their turnover frequencies, are qualitatively comparable to MOFs with experimentally demonstrated C−H activation reactivity. Nevertheless, our review of the original and related manuscripts describing these MOFs confirms that they have yet to be studied experimentally or computationally for catalysis. Thus, these previously synthesized MOFs, which

https://doi.org/10.1021/jacs.3c03351
J. Am. Chem. Soc. XXXX, XXX, XXX−XXX

are also predicted to have the stability required for thermal catalysis, are expected to have favorable kinetics for methane-to-methanol catalysis, motivating further experimental study.

4. COMPUTATIONAL DETAILS

We obtained crystallographic information files (CIFs) of all candidate MOFs from the 2019 CoRE ASR MOF database v.1.1.2[79] and used MOFSimplify[76] to extract the SBUs of each MOF. These extracted SBUs comprised the transition metals and their first and second coordination spheres, in addition to any rings that are directly coordinated to a transition metal (Supporting Information Text S4 and Figure S19). We used atomic-weighted molecular graph determinants[83] of the SBUs to identify unique MOF SBUs. We then capped these SBUs with common truncated forms of linkers, such as acetate or formate,[48] using a custom script in molSimplify[105] to generate cluster models for density functional theory (DFT) calculations (Supporting Information Table S6, Text S4, and Figures S20 and S21). As described in Section 2.2, to avoid magnetic coupling between adjacent transition-metal centers, SBUs with multiple transition-metal centers were modified by replacing all but one transition-metal center with closed-shell Mg(II) ions (Supporting Information Tables S4−S6 and Figure S3). We verified trends were unchanged with this approach in comparison to calculations in which all metal centers were kept in the SBU (Supporting Information Table S5). This created multiple instances of the same SBU with the active site position varying across all valid open metal sites and symmetrically equivalent SBUs were eliminated using atomic-weighted SBU molecular graph determinants recomputed after metal substitution.

All gas-phase geometry optimizations on the MOF cluster models were performed using DFT with a development version of TeraChem v1.9.[106,107] Cartesian constraints were applied on the first and second coordination sphere atoms from the metal to mimic the constrained ligand environment of a MOF stemming from its extended framework. The B3LYP[108−110] global hybrid functional was employed with the empirical D3 dispersion correction[111] using Becke−Johnson damping.[112] The LACVP* composite basis set was used for all calculations, which consists of a LANL2DZ effective core potential[113,114] for transition metals and the 6−31G* basis set[115] for all other atoms (Supporting Information Figure S22). All calculations were carried out in an unrestricted formalism with level-shifting[116] of 0.25 Ha applied to both majority- and minority-spin virtual orbitals to aid self-consistent field (SCF) convergence (Supporting Information Text S5 and Figure S23). Geometry optimizations were performed with the translation rotation internal coordinate (TRIC) optimizer[117] using the BFGS algorithm with default convergence thresholds of maximum energy gradient of 4.5×10^{-4} hartree/bohr and energy difference between steps of 10^{-6} hartree.

Metal-oxo geometries were generated using a custom script in molSimplify by adding an oxygen atom at the active site moiety in the MOF cluster (Supporting Information Text S6 and Figure S24). The DFT geometry optimization workflow begins by optimizing the metal-oxo geometry, and if this or any subsequent intermediate calculation fails, downstream intermediate optimizations are not attempted. From the optimized metal-oxo geometry, we followed protocols adapted from prior work[75] to functionalize the metal-oxo structure with a hydrogen atom to generate initial structures for the metal-hydroxo species and removed the oxo moiety to generate initial structures for the resting state. Initial structures of the methanol-bound species were generated by adding a methyl group to the optimized metal-hydroxo structure (Supporting Information Figure S24).

Submission of jobs was automated by molSimplify[105,118] with a 96-h wall-time limit per run with up to five resubmissions. Open-shell calculations that failed any of the following checks[74,119,120] were eliminated from the entire dataset: if the expected value of the $\hat{S}^2$ operator deviated from its expected value of $S(S + 1)$ by >1 μ_B^2 for SBUs with only one metal center and >1.1 μ_B^2 for SBUs with more than one metal center or the combined Mulliken spin density on the metal and the oxygen in the active site moiety differed from the total spin by >1 μ_B. Structures whose final geometries were unreasonably distorted as observed by visual inspection were also eliminated (Supporting Information Table S16).

Multiwfn[121] was used to obtain electronic properties of the metal-oxo intermediate such as the Mulliken spin density for the oxygen atom, the metal-oxo Mayer bond order, and the oxygen Mayer bond valence, which is the sum of the bond order between the oxygen atom and the transition metal. We selected the Mulliken population analysis due to its simplicity and low computational cost while Mayer bond order analysis was used because of its ability to describe bonding in systems with unpaired electrons. For comparison, Multiwfn was also used to perform a Lowdin population analysis and Wiberg bond order analysis to obtain the relevant metal-oxo electronic properties and we observe that qualitative trends remain the same (Supporting Information Figures S5 and S7).

Free energy landscapes of select Mn MOF SBU clusters were obtained using ORCA v5.0.1[122] with the B3LYP functional with D3 dispersion correction using the Becke−Johnson damping and the LACVP* basis set. Cartesian constraints to mimic MOF rigidity were employed. Starting from TeraChem-optimized structures, we completed additional DFT geometry optimizations to obtain thermochemical corrections on the intermediates. We employed ORCA for the free energy landscape calculations because TeraChem does not support analytical Hessians. Transition states were optimized in two steps. First, potential energy surface (PES) scans were computed where the presumed transition state mode, such as a bond length or bond angle, was incrementally changed and fixed while geometry optimizing all other degrees of freedom excluding the first and second coordination sphere atoms of the metals. The maxima from these PES scans were used as initial guesses for a partitioned rational-function optimization (P-RFO)[123] to locate the transition state structures (Supporting Information Texts S2 and S3). Transition state identities were verified by performing frequency calculations to ensure that an imaginary frequency corresponding to the expected transition state mode was observed among other small imaginary frequencies associated with the imposed constraints.[124]

All mechanical properties for select Mn MOFs were calculated using the LAMMPS molecular simulation package.[125] We extracted the moduli of elasticity from the 6×6 stiffness matrix[126] containing all information about the mechanical properties of a material in the elastic regime of the stress−strain curve. We calculate the stiffness matrix by applying a maximum strain of 1% and evaluating the relative energy difference between the deformed structure and the initial structure. All initial structures used for mechanical

https://doi.org/10.1021/jacs.3c03351
J. Am. Chem. Soc. XXXX, XXX, XXX−XXX

property calculations had optimized and relaxed cells. Mechanical property calculations used the UFF4MOF[127,128] force field with conjugate gradient minimization for geometry optimization.

■ ASSOCIATED CONTENT

Supporting Information

The Supporting Information is available free of charge at https://pubs.acs.org/doi/10.1021/jacs.3c03351.

Catalysis-specific keywords used for text parsing MOF manuscripts; representative manuscripts with and without MOF catalysis discussion; ground truth TGA statistics for stable CoRE MOFs not studied for catalysis; geometry index distributions for 4- and 5-coordinate metal sites in SBUs; FSR distribution for all metal pairs in open site SBUs; MOF screening filters based on practical considerations; coupling constants on representative multimetallic SBUs; ΔE(oxo) comparison with and without Mg(II) substitution; spin density plots of a few intermediates from broken symmetry DFT; counts of SBUs retained at each step of workflow after screening for open metal sites; shifts in ΔE(oxo) when using oxidants other than O_2; active metal oxidation state assignment in MOFs for DFT; oxidation and spin states of active metal in different intermediates; grouping of ΔE(oxo) by resting state metal coordination number; ΔE(oxo) vs metal-oxo Mayer bond order; metal-oxo bond length vs oxygen Mayer bond valence in oxo intermediates; ΔE(oxo) and ΔE(HAT) vs metal-oxo oxygen Mayer bond valence and spin density; ΔE(oxo) and ΔE(HAT) vs energetic HOMO in resting and oxo intermediates; reaction energetics scatter plots showing Fe-MOF-74 SBU energetics; comparison of ΔE(oxo) of Fe-MOF-74 SBU in this work with literature; stability metrics for DADLEC, EBUREA, and LUSHOX04; computational details on transition state searching; job rescue using spin projection on free energy landscape structures; spin projection results on Mn MOF reaction coordinates at B3LYP-D3/LACVP*; spin projection results on Mn MOF reaction coordinates at B3LYP-D3/def2-TZVPP; raw free energy landscapes with N_2O; IRC path for oxo formation using N_2O on DADLEC; IRC path for oxo formation using N_2O on LUSHOX04; free energy landscape of EBUREA with N_2O; IRC path for oxo formation using N_2O on EBUREA; free energy landscapes of DADLEC, EBUREA and LUSHOX04 with O_2; IRC path for oxo formation using O_2 with CO co-reductant on DADLEC; IRC path for superoxo and CO complexation on LUSHOX04; IRC path for O-O cleavage from superoxo-CO complex on EBUREA; representative IRC path for HAT on LUSHOX04; energetic span analysis; discussion on preparing SBU cluster models for DFT; custom modifications made to SBU clusters after MOFSimplify SBU extraction; comparison of linker-like anions of different sizes for SBU capping; SBU capping methods; basis set sensitivity of ΔE(oxo), ΔE(HAT), and ΔE(release); computational details on job rescue; metal-oxo bond length scans in representative doublet mono-cupric oxo intermediates; discussion on generation of intermediates; and illustration of intermediate generation; DFT job statistics on SBUs (PDF)

Optimized structures of all reactive intermediates for each SBU in the final MOF dataset; approximate transition state structures from the reaction coordinates; raw electronic energies and reaction energies for all SBUs in the final MOF dataset; electronic properties of all intermediates for each SBU in the final MOF dataset; SBUs that were discarded during screening or DFT; and stable single-metal Mn, Fe, Co, and Cu CoRE MOFs not studied for catalysis (ZIP)

■ AUTHOR INFORMATION

Corresponding Author

Heather J. Kulik − *Department of Chemical Engineering, Massachusetts Institute of Technology, Cambridge, Massachusetts 02139, United States; Department of Chemistry, Massachusetts Institute of Technology, Cambridge, Massachusetts 02139, United States;* orcid.org/0000-0001-9342-0191; Email: hjkulik@mit.edu

Authors

Husain Adamji − *Department of Chemical Engineering, Massachusetts Institute of Technology, Cambridge, Massachusetts 02139, United States;* orcid.org/0000-0003-3058-680X

Aditya Nandy − *Department of Chemical Engineering, Massachusetts Institute of Technology, Cambridge, Massachusetts 02139, United States; Department of Chemistry, Massachusetts Institute of Technology, Cambridge, Massachusetts 02139, United States;* orcid.org/0000-0001-7137-5449

Ilia Kevlishvili − *Department of Chemical Engineering, Massachusetts Institute of Technology, Cambridge, Massachusetts 02139, United States*

Yuriy Román-Leshkov − *Department of Chemical Engineering, Massachusetts Institute of Technology, Cambridge, Massachusetts 02139, United States; Department of Chemistry, Massachusetts Institute of Technology, Cambridge, Massachusetts 02139, United States;* orcid.org/0000-0002-0025-4233

Complete contact information is available at: https://pubs.acs.org/10.1021/jacs.3c03351

Notes

The authors declare no competing financial interest.

■ ACKNOWLEDGMENTS

This work was primarily supported by the National Science Foundation under grant number CBET-1846426 (to H.A., A.N., and H.J.K.). The authors also acknowledge support by DARPA (grant number D18AP00039) for work on curating the MOF dataset (to H.A., A.N., and H.J.K.). This work was also partially supported by a National Science Foundation Graduate Research Fellowship under Grant #1122374 (to A.N.). This work was also supported by the US Department of Energy, Office of Basic Energy Sciences under Award DE-SC0016214 (for H.A. and Y.R.-L.). This work used Expanse at San Diego Supercomputing Center through allocation CHE140073 from the Advanced Cyberinfrastructure Coordination Ecosystem: Services and Support (ACCESS) program, which is supported by National Science Foundation Grants #2138259, #2138286, #2138307, #2137603, and #2138296. H.J.K. holds an Alfred P. Sloan Fellowship in Chemistry, which

https://doi.org/10.1021/jacs.3c03351
J. Am. Chem. Soc. XXXX, XXX, XXX−XXX

supported this work. The authors thank Adam H. Steeves and David W. Kastner for providing a critical reading of the manuscript.

REFERENCES

(1) Lunsford, J. H. Catalytic Conversion of Methane to More Useful Chemicals and Fuels: A Challenge for the 21st Century. *Catal. Today* **2000**, *63*, 165−174.
(2) Olah, G. A. Beyond Oil and Gas: The Methanol Economy. *Angew. Chem., Int. Ed.* **2005**, *44*, 2636−2639.
(3) Nandy, A.; Adamji, H.; Kastner, D. W.; Vennelakanti, V.; Nazemi, A.; Liu, M.; Kulik, H. J. Using Computational Chemistry To Reveal Nature's Blueprints for Single-Site Catalysis of C−H Activation. *ACS Catal.* **2022**, *12*, 9281−9306.
(4) Kondratenko, E. V.; Peppel, T.; Seeburg, D.; Kondratenko, V. A.; Kalevaru, N.; Martin, A.; Wohlrab, S. Methane Conversion into Different Hydrocarbons or Oxygenates: Current Status and Future Perspectives in Catalyst Development and Reactor Operation. *Catal. Sci. Technol.* **2017**, *7*, 366−381.
(5) Shilov, A. E.; Shul'pin, G. B. Activation of C−H Bonds by Metal Complexes. *Chem. Rev.* **1997**, *97*, 2879−2932.
(6) Dinh, K. T.; Sullivan, M. M.; Serna, P.; Meyer, R. J.; Dincă, M.; Román-Leshkov, Y. Viewpoint on the Partial Oxidation of Methane to Methanol Using Cu- and Fe-Exchanged Zeolites. *ACS Catal.* **2018**, *8*, 8306−8313.
(7) Zichittella, G.; Pérez-Ramírez, J. Status and Prospects of the Decentralised Valorisation of Natural Gas into Energy and Energy Carriers. *Chem. Soc. Rev.* **2021**, *50*, 2984−3012.
(8) McFarland, E. Unconventional Chemistry for Unconventional Natural Gas. *Science* **2012**, *338*, 340−342.
(9) Horn, R.; Schlögl, R. Methane Activation by Heterogeneous Catalysis. *Catal. Lett.* **2015**, *145*, 23−39.
(10) Ravi, M.; Ranocchiari, M.; van Bokhoven, J. A. The Direct Catalytic Oxidation of Methane to Methanol—A Critical Assessment. *Angew. Chem., Int. Ed.* **2017**, *56*, 16464−16483.
(11) Ross, M. O.; Rosenzweig, A. C. A Tale of Two Methane Monooxygenases. *JBIC, J. Biol. Inorg. Chem.* **2017**, *22*, 307−319.
(12) Tinberg, C. E.; Lippard, S. J. Dioxygen Activation in Soluble Methane Monooxygenase. *Acc. Chem. Res.* **2011**, *44*, 280−288.
(13) Solomon, E. I.; Brunold, T. C.; Davis, M. I.; Kemsley, J. N.; Lee, S.-K.; Lehnert, N.; Neese, F.; Skulan, A. J.; Yang, Y.-S.; Zhou, J. Geometric and Electronic Structure/Function Correlations in Non-Heme Iron Enzymes. *Chem. Rev.* **2000**, *100*, 235−350.
(14) Castillo, R. G.; Banerjee, R.; Allpress, C. J.; Rohde, G. T.; Bill, E.; Que, L., Jr.; Lipscomb, J. D.; DeBeer, S. High-Energy-Resolution Fluorescence-Detected X-ray Absorption of the Q Intermediate of Soluble Methane Monooxygenase. *J. Am. Chem. Soc.* **2017**, *139*, 18024−18033.
(15) Cutsail, G. E., III; Banerjee, R.; Zhou, A.; Que, L., Jr.; Lipscomb, J. D.; DeBeer, S. High-Resolution Extended X-ray Absorption Fine Structure Analysis Provides Evidence for a Longer Fe···Fe Distance in the Q Intermediate of Methane Monooxygenase. *J. Am. Chem. Soc.* **2018**, *140*, 16807−16820.
(16) Schulz, C. E.; Castillo, R. G.; Pantazis, D. A.; DeBeer, S.; Neese, F. Structure−Spectroscopy Correlations for Intermediate Q of Soluble Methane Monooxygenase: Insights from QM/MM Calculations. *J. Am. Chem. Soc.* **2021**, *143*, 6560−6577.
(17) Nam, W. Synthetic Mononuclear Nonheme Iron−Oxygen Intermediates. *Acc. Chem. Res.* **2015**, *48*, 2415−2423.
(18) Engelmann, X.; Monte-Pérez, I.; Ray, K. Oxidation Reactions with Bioinspired Mononuclear Non-Heme Metal−Oxo Complexes. *Angew. Chem., Int. Ed.* **2016**, *55*, 7632−7649.
(19) Sader, S.; Miliordos, E. Being Negative Can Be Positive: Metal Oxide Anions Promise More Selective Methane to Methanol Conversion. *Phys. Chem. Chem. Phys.* **2022**, *24*, 21583−21587.
(20) Que, L.; Tolman, W. B. Biologically Inspired Oxidation Catalysis. *Nature* **2008**, *455*, 333−340.
(21) Wang, V. C. C.; Maji, S.; Chen, P. P. Y.; Lee, H. K.; Yu, S. S. F.; Chan, S. I. Alkane Oxidation: Methane Monooxygenases, Related Enzymes, and Their Biomimetics. *Chem. Rev.* **2017**, *117*, 8574−8621.
(22) Claveau, E. E.; Sader, S.; Jackson, B. A.; Khan, S. N.; Miliordos, E. Transition Metal Oxide Complexes as Molecular Catalysts for Selective Methane to Methanol Transformation: Any Prospects or Time to Retire? *Phys. Chem. Chem. Phys.* **2023**, *25*, 5313−5326.
(23) Snyder, B. E. R.; Bols, M. L.; Schoonheydt, R. A.; Sels, B. F.; Solomon, E. I. Iron and Copper Active Sites in Zeolites and Their Correlation to Metalloenzymes. *Chem. Rev.* **2018**, *118*, 2718−2768.
(24) Narsimhan, K.; Iyoki, K.; Dinh, K.; Román-Leshkov, Y. Catalytic Oxidation of Methane into Methanol over Copper-Exchanged Zeolites with Oxygen at Low Temperature. *ACS Cent. Sci.* **2016**, *2*, 424−429.
(25) Osadchii, D. Y.; Olivos-Suarez, A. I.; Szécsényi, Á.; Li, G.; Nasalevich, M. A.; Dugulan, I. A.; Crespo, P. S.; Hensen, E. J. M.; Veber, S. L.; Fedin, M. V.; Sankar, G.; Pidko, E. A.; Gascon, J. Isolated Fe Sites in Metal Organic Frameworks Catalyze the Direct Conversion of Methane to Methanol. *ACS Catal.* **2018**, *8*, 5542−5548.
(26) Yang, D.; Gates, B. C. Catalysis by Metal Organic Frameworks: Perspective and Suggestions for Future Research. *ACS Catal.* **2019**, *9*, 1779−1798.
(27) Lee, J.; Farha, O. K.; Roberts, J.; Scheidt, K. A.; Nguyen, S. T.; Hupp, J. T. Metal-Organic Framework Materials as Catalysts. *Chem. Soc. Rev.* **2009**, *38*, 1450−1459.
(28) Rogge, S. M. J.; Bavykina, A.; Hajek, J.; Garcia, H.; Olivos-Suarez, A. I.; Sepúlveda-Escribano, A.; Vimont, A.; Clet, G.; Bazin, P.; Kapteijn, F.; Daturi, M.; Ramos-Fernandez, E. V.; Llabrés i Xamena, F. X.; Van Speybroeck, V.; Gascon, J. Metal-Organic and Covalent Organic Frameworks as Single-Site Catalysts. *Chem. Soc. Rev.* **2017**, *46*, 3134−3184.
(29) Wang, Z.; Bilegsaikhan, A.; Jerozal, R. T.; Pitt, T. A.; Milner, P. J. Evaluating the Robustness of Metal−Organic Frameworks for Synthetic Chemistry. *ACS Appl. Mater. Interfaces* **2021**, *13*, 17517−17531.
(30) Furukawa, H.; Cordova, K. E.; O'Keeffe, M.; Yaghi, O. M. The Chemistry and Applications of Metal-Organic Frameworks. *Science* **2013**, *341*, No. 1230444.
(31) Zhou, H.-C.; Long, J. R.; Yaghi, O. M. Introduction to Metal−Organic Frameworks. *Chem. Rev.* **2012**, *112*, 673−674.
(32) Bour, J. R.; Wright, A. M.; He, X.; Dincă, M. Bioinspired Chemistry at Metal-Organic Framework (MOF) Secondary Building Units. *Chem. Sci.* **2020**, *11*, 1728−1737.
(33) Hendon, C. H.; Rieth, A. J.; Korzyński, M. D.; Dincă, M. Grand Challenges and Future Opportunities for Metal−Organic Frameworks. *ACS Cent. Sci.* **2017**, *3*, 554−563.
(34) Gherman, B. F.; Lippard, S. J.; Friesner, R. A. Substrate Hydroxylation in Methane Monooxygenase: Quantitative Modeling via Mixed Quantum Mechanics/Molecular Mechanics Techniques. *J. Am. Chem. Soc.* **2005**, *127*, 1025−1037.
(35) Snyder, B. E. R.; Vanelderen, P.; Bols, M. L.; Hallaert, S. D.; Böttger, L. H.; Ungur, L.; Pierloot, K.; Schoonheydt, R. A.; Sels, B. F.; Solomon, E. I. The Active Site of Low-Temperature Methane Hydroxylation in Iron-Containing Zeolites. *Nature* **2016**, *536*, 317−321.
(36) Snyder, B. E. R.; Böttger, L. H.; Bols, M. L.; Yan, J. J.; Rhoda, H. M.; Jacobs, A. B.; Hu, M. Y.; Zhao, J.; Alp, E. E.; Hedman, B.; Hodgson, K. O.; Schoonheydt, R. A.; Sels, B. F.; Solomon, E. I. Structural Characterization of a Non-Heme Iron Active Site in Zeolites That Hydroxylates Methane. *Proc. Natl. Acad. Sci.* **2018**, *115*, 4565−4570.
(37) Bols, M. L.; Hallaert, S. D.; Snyder, B. E. R.; Devos, J.; Plessers, D.; Rhoda, H. M.; Dusselier, M.; Schoonheydt, R. A.; Pierloot, K.; Solomon, E. I.; Sels, B. F. Spectroscopic Identification of the α-Fe/α-O Active Site in Fe-CHA Zeolite for the Low-Temperature Activation of the Methane C−H Bond. *J. Am. Chem. Soc.* **2018**, *140*, 12021−12032.

https://doi.org/10.1021/jacs.3c03351
J. Am. Chem. Soc. XXXX, XXX, XXX−XXX

(38) Xiao, D. J.; Bloch, E. D.; Mason, J. A.; Queen, W. L.; Hudson, M. R.; Planas, N.; Borycz, J.; Dzubak, A. L.; Verma, P.; Lee, K.; Bonino, F.; Crocellà, V.; Yano, J.; Bordiga, S.; Truhlar, D. G.; Gagliardi, L.; Brown, C. M.; Long, J. R. Oxidation of Ethane to Ethanol by N_2O in a Metal−Organic Framework with Coordinatively Unsaturated Iron(II) Sites. *Nat. Chem.* **2014**, *6*, 590−595.
(39) Simons, M. C.; Vitillo, J. G.; Babucci, M.; Hoffman, A. S.; Boubnov, A.; Beauvais, M. L.; Chen, Z.; Cramer, C. J.; Chapman, K. W.; Bare, S. R.; Gates, B. C.; Lu, C. C.; Gagliardi, L.; Bhan, A. Structure, Dynamics, and Reactivity for Light Alkane Oxidation of Fe(II) Sites Situated in the Nodes of a Metal−Organic Framework. *J. Am. Chem. Soc.* **2019**, *141*, 18142−18151.
(40) Simons, M. C.; Prinslow, S. D.; Babucci, M.; Hoffman, A. S.; Hong, J.; Vitillo, J. G.; Bare, S. R.; Gates, B. C.; Lu, C. C.; Gagliardi, L.; Bhan, A. Beyond Radical Rebound: Methane Oxidation to Methanol Catalyzed by Iron Species in Metal−Organic Framework Nodes. *J. Am. Chem. Soc.* **2021**, *143*, 12165−12174.
(41) Baek, J.; Rungtaweevoranit, B.; Pei, X.; Park, M.; Fakra, S. C.; Liu, Y.-S.; Matheu, R.; Alshmimri, S. A.; Alshehri, S.; Trickett, C. A.; Somorjai, G. A.; Yaghi, O. M. Bioinspired Metal−Organic Framework Catalysts for Selective Methane Oxidation to Methanol. *J. Am. Chem. Soc.* **2018**, *140*, 18208−18216.
(42) Feng, X.; Song, Y.; Chen, J. S.; Xu, Z.; Dunn, S. J.; Lin, W. Rational Construction of an Artificial Binuclear Copper Monooxygenase in a Metal−Organic Framework. *J. Am. Chem. Soc.* **2021**, *143*, 1107−1118.
(43) Zhang, X.; Huang, Z.; Ferrandon, M.; Yang, D.; Robison, L.; Li, P.; Wang, T. C.; Delferro, M.; Farha, O. K. Catalytic Chemoselective Functionalization of Methane in a Metal−Organic Framework. *Nat. Catal.* **2018**, *1*, 356−362.
(44) Dinh, K. T.; Sullivan, M. M.; Narsimhan, K.; Serna, P.; Meyer, R. J.; Dincă, M.; Román-Leshkov, Y. Continuous Partial Oxidation of Methane to Methanol Catalyzed by Diffusion-Paired Copper Dimers in Copper-Exchanged Zeolites. *J. Am. Chem. Soc.* **2019**, *141*, 11641−11650.
(45) Wiktor, C.; Meledina, M.; Turner, S.; Lebedev, O. I.; Fischer, R. A. Transmission Electron Microscopy on Metal−Organic Frameworks−A Review. *J. Mater. Chem. A* **2017**, *5*, 14969−14989.
(46) Chen, Q.; Dwyer, C.; Sheng, G.; Zhu, C.; Li, X.; Zheng, C.; Zhu, Y. Imaging Beam-Sensitive Materials by Electron Microscopy. *Adv. Mater.* **2020**, *32*, No. 1907619.
(47) Zhu, L.; Zhang, D.; Xue, M.; Li, H.; Qiu, S. Direct Observations of the MOF (UiO-66) Structure by Transmission Electron Microscopy. *CrystEngComm* **2013**, *15*, 9356−9359.
(48) Bernales, V.; Ortuño, M. A.; Truhlar, D. G.; Cramer, C. J.; Gagliardi, L. Computational Design of Functionalized Metal−Organic Framework Nodes for Catalysis. *ACS Cent. Sci.* **2018**, *4*, 5−19.
(49) Verma, P.; Vogiatzis, K. D.; Planas, N.; Borycz, J.; Xiao, D. J.; Long, J. R.; Gagliardi, L.; Truhlar, D. G. Mechanism of Oxidation of Ethane to Ethanol at Iron(IV)−Oxo Sites in Magnesium-Diluted Fe_2(dobdc). *J. Am. Chem. Soc.* **2015**, *137*, 5770−5781.
(50) Vitillo, J. G.; Lu, C. C.; Cramer, C. J.; Bhan, A.; Gagliardi, L. Influence of First and Second Coordination Environment on Structural Fe(II) Sites in MIL-101 for C−H Bond Activation in Methane. *ACS Catal.* **2021**, *11*, 579−589.
(51) Moghadam, P. Z.; Li, A.; Wiggin, S. B.; Tao, A.; Maloney, A. G. P.; Wood, P. A.; Ward, S. C.; Fairen-Jimenez, D. Development of a Cambridge Structural Database Subset: A Collection of Metal−Organic Frameworks for Past, Present, and Future. *Chem. Mater.* **2017**, *29*, 2618−2625.
(52) Moosavi, S. M.; Nandy, A.; Jablonka, K. M.; Ongari, D.; Janet, J. P.; Boyd, P. G.; Lee, Y.; Smit, B.; Kulik, H. J. Understanding the Diversity of the Metal-Organic Framework Ecosystem. *Nat. Commun.* **2020**, *11*, No. 4068.
(53) Vogiatzis, K. D.; Haldoupis, E.; Xiao, D. J.; Long, J. R.; Siepmann, J. I.; Gagliardi, L. Accelerated Computational Analysis of Metal−Organic Frameworks for Oxidation Catalysis. *J. Phys. Chem. C* **2016**, *120*, 18707−18712.
(54) Rosen, A. S.; Notestein, J. M.; Snurr, R. Q. Identifying Promising Metal-Organic Frameworks for Heterogeneous Catalysis via High-Throughput Periodic Density Functional Theory. *J. Comput. Chem.* **2019**, *40*, 1305−1318.
(55) Rosen, A. S.; Notestein, J. M.; Snurr, R. Q. Structure-Activity Relationships That Identify Metal-Organic Framework Catalysts for Methane Activation. *ACS Catal.* **2019**, *9*, 3576−3587.
(56) Barona, M.; Ahn, S.; Morris, W.; Hoover, W.; Notestein, J. M.; Farha, O. K.; Snurr, R. Q. Computational Predictions and Experimental Validation of Alkane Oxidative Dehydrogenation by Fe_2M MOF Nodes. *ACS Catal.* **2020**, *10*, 1460−1469.
(57) Barona, M.; Snurr, R. Q. Exploring the Tunability of Trimetallic MOF Nodes for Partial Oxidation of Methane to Methanol. *ACS Appl. Mater. Interfaces* **2020**, *12*, 28217−28231.
(58) Nandy, A.; Duan, C.; Kulik, H. J. Using Machine Learning and Data Mining to Leverage Community Knowledge for the Engineering of Stable Metal−Organic Frameworks. *J. Am. Chem. Soc.* **2021**, *143*, 17535−17547.
(59) Abild-Pedersen, F.; Greeley, J.; Studt, F.; Rossmeisl, J.; Munter, T. R.; Moses, P. G.; Skúlason, E.; Bligaard, T.; Nørskov, J. K. Scaling Properties of Adsorption Energies for Hydrogen-Containing Molecules on Transition-Metal Surfaces. *Phys. Rev. Lett.* **2007**, *99*, No. 016105.
(60) Greeley, J. Theoretical Heterogeneous Catalysis: Scaling Relationships and Computational Catalyst Design. *Annu. Rev. Chem. Biomol. Eng.* **2016**, *7*, 605−635.
(61) Wodrich, M. D.; Busch, M.; Corminboeuf, C. Accessing and Predicting the Kinetic Profiles of Homogeneous Catalysts from Volcano Plots. *Chem. Sci.* **2016**, *7*, 5723−5735.
(62) Latimer, A. A.; Kulkarni, A. R.; Aljama, H.; Montoya, J. H.; Yoo, J. S.; Tsai, C.; Abild-Pedersen, F.; Studt, F.; Nørskov, J. K. Understanding Trends in C-H Bond Activation in Heterogeneous Catalysis. *Nat. Mater.* **2017**, *16*, 225−229.
(63) Latimer, A. A.; Kakekhani, A.; Kulkarni, A. R.; Nørskov, J. K. Direct Methane to Methanol: The Selectivity−Conversion Limit and Design Strategies. *ACS Catal.* **2018**, *8*, 6894−6907.
(64) Calle-Vallejo, F.; Loffreda, D.; Koper, M. T. M.; Sautet, P. Introducing Structural Sensitivity into Adsorption-Energy Scaling Relations by Means of Coordination Numbers. *Nat. Chem.* **2015**, *7*, 403−410.
(65) Liao, P.; Getman, R. B.; Snurr, R. Q. Optimizing Open Iron Sites in Metal-Organic Frameworks for Ethane Oxidation: A First-Principles Study. *ACS Appl. Mater. Interfaces* **2017**, *9*, 33484−33492.
(66) Busch, M.; Wodrich, M. D.; Corminboeuf, C. Linear Scaling Relationships and Volcano Plots in Homogeneous Catalysis: Revisiting the Suzuki Reaction. *Chem. Sci.* **2015**, *6*, 6754−6761.
(67) Cordova, M.; Wodrich, M. D.; Meyer, B.; Sawatlon, B.; Corminboeuf, C. Data-Driven Advancement of Homogeneous Nickel Catalyst Activity for Aryl Ether Cleavage. *ACS Catal.* **2020**, *10*, 7021−7031.
(68) Schneider, J. E.; Goetz, M. K.; Anderson, J. S. Statistical Analysis of C-H Activation by Oxo Complexes Supports Diverse Thermodynamic Control over Reactivity. *Chem. Sci.* **2021**, *12*, 4173−4183.
(69) Pellizzeri, S.; Barona, M.; Bernales, V.; Miró, P.; Liao, P.; Gagliardi, L.; Snurr, R. Q.; Getman, R. B. Catalytic Descriptors and Electronic Properties of Single-Site Catalysts for Ethene Dimerization to 1-Butene. *Catal. Today* **2018**, *312*, 149−157.
(70) Khorshidi, A.; Violet, J.; Hashemi, J.; Peterson, A. A. How Strain Can Break the Scaling Relations of Catalysis. *Nat. Catal.* **2018**, *1*, 263−268.
(71) Andrikopoulos, P. C.; Michel, C.; Chouzier, S.; Sautet, P. In Silico Screening of Iron-Oxo Catalysts for CH Bond Cleavage. *ACS Catal.* **2015**, *5*, 2490−2499.
(72) Gani, T. Z. H.; Kulik, H. J. Understanding and Breaking Scaling Relations in Single-Site Catalysis: Methane to Methanol Conversion by Fe^{IV}=O. *ACS Catal.* **2018**, *8*, 975−986.
(73) Szécsényi, Á.; Khramenkova, E.; Chernyshov, I. Y.; Li, G.; Gascon, J.; Pidko, E. A. Breaking Linear Scaling Relationships with

https://doi.org/10.1021/jacs.3c03351
J. Am. Chem. Soc. XXXX, XXX, XXX−XXX

Secondary Interactions in Confined Space: A Case Study of Methane Oxidation by Fe/ZSM-5 Zeolite. *ACS Catal.* **2019**, *9*, 9276−9284.
(74) Nandy, A.; Zhu, J.; Janet, J. P.; Duan, C.; Getman, R. B.; Kulik, H. J. Machine Learning Accelerates the Discovery of Design Rules and Exceptions in Stable Metal−Oxo Intermediate Formation. *ACS Catal.* **2019**, *9*, 8243−8255.
(75) Nandy, A.; Kulik, H. J. Why Conventional Design Rules for C−H Activation Fail for Open-Shell Transition-Metal Catalysts. *ACS Catal.* **2020**, *10*, 15033−15047.
(76) Nandy, A.; Terrones, G.; Arunachalam, N.; Duan, C.; Kastner, D. W.; Kulik, H. J. MOFSimplify: Machine Learning Models with Extracted Stability Data of Three Thousand Metal-Organic Frameworks. *Sci. Data* **2022**, *9*, No. 74.
(77) Howarth, A. J.; Liu, Y.; Li, P.; Li, Z.; Wang, T. C.; Hupp, J. T.; Farha, O. K. Chemical, Thermal, and Mechanical Stabilities of Metal-Organic Frameworks. *Nat. Rev. Mater.* **2016**, *1*, No. 15018.
(78) Yuan, S.; Feng, L.; Wang, K.; Pang, J.; Bosch, M.; Lollar, C.; Sun, Y.; Qin, J.; Yang, X.; Zhang, P.; Wang, Q.; Zou, L.; Zhang, Y.; Zhang, L.; Fang, Y.; Li, J.; Zhou, H.-C. Stable Metal−Organic Frameworks: Design, Synthesis, and Applications. *Adv. Mater.* **2018**, *30*, No. 1704303.
(79) Chung, Y. G.; Haldoupis, E.; Bucior, B. J.; Haranczyk, M.; Lee, S.; Zhang, H.; Vogiatzis, K. D.; Milisavljevic, M.; Ling, S.; Camp, J. S.; Slater, B.; Siepmann, J. I.; Sholl, D. S.; Snurr, R. Q. Advances, Updates, and Analytics for the Computation-Ready, Experimental Metal−Organic Framework Database: CoRE MOF 2019. *J. Chem. Eng. Data* **2019**, *64*, 5985−5998.
(80) Mlekodaj, K.; Lemishka, M.; Sklenak, S.; Dedecek, J.; Tabor, E. Dioxygen Splitting at Room Temperature over Distant Binuclear Transition Metal Centers in Zeolites for Direct Oxidation of Methane to Methanol. *Chem. Commun.* **2021**, *57*, 3472−3475.
(81) Kim, E.; Huang, K.; Jegelka, S.; Olivetti, E. Virtual Screening of Inorganic Materials Synthesis Parameters with Deep Learning. *npj Comput. Mater.* **2017**, *3*, No. 53.
(82) Swain, M. C.; Cole, J. M. ChemDataExtractor: A Toolkit for Automated Extraction of Chemical Information from the Scientific Literature. *J. Chem. Inf. Model.* **2016**, *56*, 1894−1904.
(83) Taylor, M. G.; Yang, T.; Lin, S.; Nandy, A.; Janet, J. P.; Duan, C.; Kulik, H. J. Seeing Is Believing: Experimental Spin States from Machine Learning Model Structure Predictions. *J. Phys. Chem. A* **2020**, *124*, 3286−3299.
(84) Addison, A. W.; Rao, T. N.; Reedijk, J.; van Rijn, J.; Verschoor, G. C. Synthesis, Structure, and Spectroscopic Properties of Copper(II) Compounds Containing Nitrogen−Sulphur Donor Ligands; The Crystal and Molecular Structure of Aqua[1,7-Bis(N-Methylbenzimidazol-2′-yl)-2,6-Dithiaheptane]Copper(II) Perchlorate. *J. Chem. Soc., Dalton Trans.* **1984**, 1349−1356.
(85) Okuniewski, A.; Rosiak, D.; Chojnacki, J.; Becker, B. Coordination Polymers and Molecular Structures Among Complexes of Mercury(II) Halides with Selected 1-Benzoylthioureas. *Polyhedron* **2015**, *90*, 47−57.
(86) Eisenhart, R. J.; Rudd, P. A.; Planas, N.; Boyce, D. W.; Carlson, R. K.; Tolman, W. B.; Bill, E.; Gagliardi, L.; Lu, C. C. Pushing the Limits of Delta Bonding in Metal−Chromium Complexes with Redox Changes and Metal Swapping. *Inorg. Chem.* **2015**, *54*, 7579−7592.
(87) Eisenhart, R. J.; Clouston, L. J.; Lu, C. C. Configuring Bonds Between First-Row Transition Metals. *Acc. Chem. Res.* **2015**, *48*, 2885−2894.
(88) Øien-Ødegaard, S.; Shearer, G. C.; Wragg, D. S.; Lillerud, K. P. Pitfalls in Metal-Organic Framework Crystallography: Towards More Accurate Crystal Structures. *Chem. Soc. Rev.* **2017**, *46*, 4867−4876.
(89) Groves, J. T.; McClusky, G. A. Aliphatic Hydroxylation via Oxygen Rebound. Oxygen Transfer Catalyzed by Iron. *J. Am. Chem. Soc.* **1976**, *98*, 859−861.
(90) Ballhausen, C. J.; Gray, H. B. The Electronic Structure of the Vanadyl Ion. *Inorg. Chem.* **1962**, *1*, 111−122.
(91) Latimer, A. A.; Aljama, H.; Kakekhani, A.; Yoo, J. S.; Kulkarni, A.; Tsai, C.; Garcia-Melchor, M.; Abild-Pedersen, F.; Nørskov, J. K. Mechanistic Insights into Heterogeneous Methane Activation. *Phys. Chem. Chem. Phys.* **2017**, *19*, 3575−3581.
(92) Nandy, A.; Duan, C.; Goffinet, C.; Kulik, H. J. New Strategies for Direct Methane-to-Methanol Conversion from Active Learning Exploration of 16 Million Catalysts. *JACS Au* **2022**, *2*, 1200−1213.
(93) Mayer, I. Bond Order and Valence Indices: A Personal Account. *J. Comput. Chem.* **2007**, *28*, 204−221.
(94) Vennelakanti, V.; Nandy, A.; Kulik, H. J. The Effect of Hartree-Fock Exchange on Scaling Relations and Reaction Energetics for C-H Activation Catalysts. *Top. Catal.* **2022**, *65*, 296−311.
(95) Kulkarni, A. R.; Zhao, Z.-J.; Siahrostami, S.; Nørskov, J. K.; Studt, F. Cation-Exchanged Zeolites for the Selective Oxidation of Methane to Methanol. *Catal. Sci. Technol.* **2018**, *8*, 114−123.
(96) He, Y.-P.; Yuan, L.-B.; Xu, H.; Zhang, J. Control of Interpenetration and Gas-Sorption Properties of Three Mn(II)-tris((4-carboxyl)phenylduryl)amine Frameworks by Tuning Solvent and Temperature. *Cryst. Growth Des.* **2017**, *17*, 290−294.
(97) Meng, M.; Zhong, D.-C.; Lu, T.-B. Three Porous Metal-Organic Frameworks Based on an Azobenzenetricarboxylate Ligand: Synthesis, Structures, and Magnetic Properties. *CrystEngComm* **2011**, *13*, 6794−6800.
(98) Asha, K. S.; Ranjith, K. M.; Yogi, A.; Nath, R.; Mandal, S. Magnetic Properties of Manganese-Based One-Dimensional Spin Chains. *Dalton Trans.* **2015**, *44*, 19812−19819.
(99) Nandy, A.; Yue, S.; Oh, C.; Duan, C.; Terrones, G. G.; Chung, Y. G.; Kulik, H. J. A Database of Ultrastable MOFs Reassembled from Stable Fragments with Machine Learning Models. *Matter* **2023**, *6*, 1585−1603.
(100) Bols, M. L.; Snyder, B. E. R.; Rhoda, H. M.; Cnudde, P.; Fayad, G.; Schoonheydt, R. A.; Van Speybroeck, V.; Solomon, E. I.; Sels, B. F. Coordination and Activation of Nitrous Oxide by Iron Zeolites. *Nat. Catal.* **2021**, *4*, 332−340.
(101) Tabor, E.; Dedecek, J.; Mlekodaj, K.; Sobalik, Z.; Andrikopoulos, P. C.; Sklenak, S. Dioxygen Dissociation over Man-Made System at Room Temperature to Form the Active α-Oxygen for Methane Oxidation. *Sci. Adv.* **2020**, *6*, No. eaaz9776.
(102) Tabor, E.; Lemishka, M.; Olszowka, J. E.; Mlekodaj, K.; Dedecek, J.; Andrikopoulos, P. C.; Sklenak, S. Splitting Dioxygen over Distant Binuclear Fe Sites in Zeolites. Effect of the Local Arrangement and Framework Topology. *ACS Catal.* **2021**, *11*, 2340−2355.
(103) Kozuch, S.; Shaik, S. How to Conceptualize Catalytic Cycles? The Energetic Span Model. *Acc. Chem. Res.* **2011**, *44*, 101−110.
(104) Vitillo, J. G.; Bhan, A.; Cramer, C. J.; Lu, C. C.; Gagliardi, L. Quantum Chemical Characterization of Structural Single Fe(II) Sites in MIL-Type Metal−Organic Frameworks for the Oxidation of Methane to Methanol and Ethane to Ethanol. *ACS Catal.* **2019**, *9*, 2870−2879.
(105) Ioannidis, E. I.; Gani, T. Z.; Kulik, H. J. molSimplify: A Toolkit for Automating Discovery in Inorganic Chemistry. *J. Comput. Chem.* **2016**, *37*, 2106−2117.
(106) Seritan, S.; Bannwarth, C.; Fales, B. S.; Hohenstein, E. G.; Isborn, C. M.; Kokkila-Schumacher, S. I. L.; Li, X.; Liu, F.; Luehr, N.; Snyder, J. W., Jr.; Song, C.; Titov, A. V.; Ufimtsev, I. S.; Wang, L.-P.; Martínez, T. J. TeraChem: A Graphical Processing Unit-Accelerated Electronic Structure Package for Large-Scale Ab Initio Molecular Dynamics. *Wiley Interdiscip. Rev.: Comput. Mol. Sci.* **2021**, *11*, No. e1494.
(107) Petachem. TeraChem. http://www.petachem.com (accessed July 25, 2022).
(108) Becke, A. D. Density-Functional Thermochemistry. III. The Role of Exact Exchange. *J. Chem. Phys.* **1993**, *98*, 5648−5652.
(109) Lee, C.; Yang, W.; Parr, R. G. Development of the Colle-Salvetti Correlation-Energy Formula into a Functional of the Electron Density. *Phys. Rev. B* **1988**, *37*, 785−789.
(110) Stephens, P. J.; Devlin, F. J.; Chabalowski, C. F.; Frisch, M. J. Ab Initio Calculation of Vibrational Absorption and Circular Dichroism Spectra Using Density Functional Force Fields. *J. Phys. Chem. A* **1994**, *98*, 11623−11627.

https://doi.org/10.1021/jacs.3c03351
J. Am. Chem. Soc. XXXX, XXX, XXX−XXX

(111) Grimme, S.; Antony, J.; Ehrlich, S.; Krieg, H. A Consistent and Accurate Ab Initio Parametrization of Density Functional Dispersion Correction (DFT-D) for the 94 Elements H-Pu. *J. Chem. Phys.* **2010**, *132*, No. 154104.
(112) Becke, A. D.; Johnson, E. R. A Density-Functional Model of the Dispersion Interaction. *J. Chem. Phys.* **2005**, *123*, No. 154101.
(113) Wadt, W. R.; Hay, P. J. Ab Initio Effective Core Potentials for Molecular Calculations. Potentials for Main Group Elements Na to Bi. *J. Chem. Phys.* **1985**, *82*, 284−298.
(114) Hay, P. J.; Wadt, W. R. Ab Initio Effective Core Potentials for Molecular Calculations: Potentials for the Transition Metal Atoms Sc to Hg. *J. Chem. Phys.* **1985**, *82*, 270−283.
(115) Rassolov, V. A.; Pople, J. A.; Ratner, M. A.; Windus, T. L. 6-31G* Basis Set for Atoms K Through Zn. *J. Chem. Phys.* **1998**, *109*, 1223−1229.
(116) Saunders, V. R.; Hillier, I. H. A "Level−Shifting" Method for Converging Closed Shell Hartree−Fock Wave Functions. *Int. J. Quantum Chem.* **1973**, *7*, 699−705.
(117) Wang, L.-P.; Song, C. Geometry Optimization Made Simple with Translation and Rotation Coordinates. *J. Chem. Phys.* **2016**, *144*, No. 214108.
(118) Group, K. molSimplify & molSimplify Automatic Design. https://github.com/hjkgrp/molsimplify (accessed July 25, 2022).
(119) Duan, C.; Janet, J. P.; Liu, F.; Nandy, A.; Kulik, H. J. Learning from Failure: Predicting Electronic Structure Calculation Outcomes with Machine Learning Models. *J. Chem. Theory Comput.* **2019**, *15*, 2331−2345.
(120) Nandy, A.; Duan, C.; Janet, J. P.; Gugler, S.; Kulik, H. J. Strategies and Software for Machine Learning Accelerated Discovery in Transition Metal Chemistry. *Ind. Eng. Chem. Res.* **2018**, *57*, 13973−13986.
(121) Lu, T.; Chen, F. Multiwfn: A Multifunctional Wavefunction Analyzer. *J. Comput. Chem.* **2012**, *33*, 580−592.
(122) Neese, F. Software Update: The ORCA Program System—Version 5.0. *Wiley Interdiscip. Rev.: Comput. Mol. Sci.* **2022**, *12*, No. e1606.
(123) Baker, J. An Algorithm for the Location of Transition States. *J. Comput. Chem.* **1986**, *7*, 385−395.
(124) Mancuso, J. L.; Mroz, A. M.; Le, K. N.; Hendon, C. H. Electronic Structure Modeling of Metal−Organic Frameworks. *Chem. Rev.* **2020**, *120*, 8641−8715.
(125) Thompson, A. P.; Aktulga, H. M.; Berger, R.; Bolintineanu, D. S.; Brown, W. M.; Crozier, P. S.; in't Veld, P. J.; Kohlmeyer, A.; Moore, S. G.; Nguyen, T. D.; et al. LAMMPS-A Flexible Simulation Tool for Particle-Based Materials Modeling at the Atomic, Meso, and Continuum Scales. *Comput. Phys. Commun.* **2022**, *271*, No. 108171.
(126) Mouhat, F.; Coudert, F.-X. Necessary and Sufficient Elastic Stability Conditions in Various Crystal Systems. *Phys. Rev. B* **2014**, *90*, No. 224104.
(127) Addicoat, M. A.; Vankova, N.; Akter, I. F.; Heine, T. Extension of the Universal Force Field to Metal−Organic Frameworks. *J. Chem. Theory Comput.* **2014**, *10*, 880−891.
(128) Coupry, D. E.; Addicoat, M. A.; Heine, T. Extension of the Universal Force Field for Metal−Organic Frameworks. *J. Chem. Theory Comput.* **2016**, *12*, 5215−5225.

https://doi.org/10.1021/jacs.3c03351
J. Am. Chem. Soc. XXXX, XXX, XXX−XXX